ADVANCED MATERIALS
www.advmat.de

Ion-Reconfigurable "N"-Shaped Antiambipolar Behavior in Organic Electrochemical Transistors

Debdatta Panigrahi, Daniele Zucchelli, Zeinab Hamid, Christina Kousseff, Arup Sarkar, Aristea Pavlou, Zhitian Ling, Somayeh Kashani, Iain McCulloch, Paul W. M. Blom, Fabrizio Toricelli, and Paschalis Gkoupidenis**

"N"-shaped negative differential transconductance (NDT) is crucial for advanced electronic applications, including neuromorphic circuits, multivalued logic, and Logic-in-Memory devices. Organic electrochemical transistors (OECTs) offer an energy-efficient platform for these technologies, yet achieving NDT behavior in single-material OECTs remains challenging. In this study, the realization of "N"-shaped transfer characteristics in OECTs is demonstrated by combining the p(C_4DPP-T) polymer with a potassium iodide (KI) electrolyte. The emergence of this unique behavior is attributed to the distinctive electrochemical properties of iodide, including its ability to participate in redox reactions and form triiodide species. Notably, this behavior emerges exclusively with iodide ions, while chloride, bromide and several other anions induce conventional monotonic p-type characteristics. By systematically tuning polymer microstructure, electrolyte concentration, and gate voltage scan rates, the intricate interplay among polymer-iodide interactions, and charge transport is uncovered, optimizing critical performance parameters such as the peak-to-valley ratio and the NDT range. Additionally, how iodine (I^-) concentration effectively facilitates ion-driven reconfigurability in OECT-based circuits, enabling transitions between binary and ternary logic states is illustrated. The results highlight an unprecedented tunability of NDT behavior in OECTs and hold immense promise for the advancement of NDT-OECTs in next-generation electronic and neuromorphic applications.

1. Introduction

Negative Differential Transconductance (NDT) in organic transistors is an intriguing phenomenon where the drain current (I_{DS}) initially increases with increasing gate voltage (V_{GS}), but after reaching a peak, I_{DS} begins to decrease, resulting in a distinctive "Λ"-shaped transfer curve.[1–9] Transistors exhibiting this behavior are often referred to as antiambipolar transistors (AATs) due to their "Λ"-shaped response, which contrasts sharply with the "V"-shaped characteristics of the ambipolar transistors. This unique NDT behavior of AATs has been explored for a range of device applications, including neuromorphic devices, and reconfigurable logic circuits.[10–14]

Recent research has predominantly focused on p-n heterojunction-based organic field-effect transistors (OFETs) that exhibit antiambipolar behavior.[1–5,10–14] However, inducing NDT in OFETs typically requires high operating voltages, ranging from 5 to 60 V, which increases power consumption and limits their practical

D. Panigrahi, A. Sarkar, A. Pavlou, Z. Ling, P. W. M. Blom, P. Gkoupidenis
Department of Molecular Electronics
Max Planck Institute for Polymer Research
55128 Mainz, Germany
E-mail: panigrahid@mpip-mainz.mpg.de; pgkoupi@ncsu.edu
D. Zucchelli, F. Toricelli
Department of Information Engineering
University of Brescia
Via Branze 38, Brescia 25123, Italy

The ORCID identification number(s) for the author(s) of this article can be found under https://doi.org/10.1002/adma.202516684

DOI: 10.1002/adma.202516684

Z. Hamid, C. Kousseff, I. McCulloch
Department of Chemistry
University of Oxford
12 Mansfield Road, Oxford OX1 3TA, UK
S. Kashani, P. Gkoupidenis
Department of Electrical and Computer Engineering
North Carolina State University
890 Oval Dr, Raleigh, NC 27606, USA
S. Kashani, P. Gkoupidenis
Carbon Electronics Laboratories (ORaCEL)
North Carolina State University
Raleigh, NC 27695, USA
I. McCulloch
Department of Electrical and Computer Engineering
Princeton University
41 Olden Street, Princeton, NJ 08544-0001, USA
P. Gkoupidenis
Department of Physics
North Carolina State University
2401 Stinson Dr, Raleigh, NC 27607, USA

applicability.[10,11] In contrast, organic electrochemical transistors (OECTs) offer a promising alternative, operating at much lower voltages (typically below 1 V), thereby significantly reducing power consumption. Furthermore, unlike OFETs, OECTs can exhibit NDT behavior using a single semiconducting polymer, simplifying the fabrication process by eliminating the need for p-n heterojunctions.[15–19]

Although "Λ"-shaped transfer curves have been demonstrated in OECTs, which show promise in reconfigurable electronics and artificial neurons, this form of NDT presents limitations for certain advanced applications.[17–26] For instance, developing full-swing multi-state logic circuits and Logic-in-Memory devices require an N-shaped antiambipolar behavior, as the second I_{DS} enhancement region beyond NDT is necessary to achieve a complete supply voltage to ground voltage swing.[27–33] Additionally, in artificial spiking neurons, an N-shaped (or S-shaped) curve is required for inducing electrochemical instabilities necessary for the implementation of artificial spiking neurons.[34–37] While p-n junction-based OFETs have achieved this behavior by altering geometry of the p-n heterojunction, the realization of N-shaped curves in OECTs still remains limited.[27,38,39]

A recent study by Tjhe et al. showed N-shaped transfer curves in OECTs using a p-type polymer, indacenodithiophene-co-benzothiadiazole (IDT-BT), in conjugation with a solid, non-aqueous ion gel electrolyte. The devices operated at a low V_{GS} of 1.5 V, and the N-shaped behavior was attributed to a band-filling mechanism.[40] While this study marked a significant advancement, it emphasized the need for further research involving various polymer–electrolyte systems, particularly those in aqueous environments which are well-suited for neuromorphic applications oriented to bioelectronics, to broaden the understanding of NDT behavior and to uncover alternative mechanisms. Additionally, it is essential to identify and control the key parameters influencing NDT behavior, including kinetic factors such as gate voltage scan rate and ion type and concentration, as well as morphological factors like polymer microstructure, which govern ion transport and interfacial interactions. Such investigations are crucial for the rational design and optimization of NDT-OECTs, tailored to support a broader range of advanced electronic applications.

In this work, we introduce an N-shaped antiambipolar behavior in OECTs using a combination of the p(C_4DPP-T) polymer and an aqueous solution of potassium iodide (KI) as the liquid-state electrolyte. The use of an aqueous electrolyte not only makes the devices more practical for neuromorphic applications but also facilitates operation at very low voltages (300 mV). The observed NDT effect is attributed to the redox activity and triiodide-forming capability of iodide ions. Additionally, we explore the influence of polymer annealing conditions, KI concentration, and V_{GS} scan rate on the NDT behavior to better understand and control polymer-electrolyte interactions. These investigations allowed us to achieve high peak-to-valley ratio (PVR) and broaden the negative differential transconductance range (NDTR). High PVR ensures greater distinguishability between peak and valley currents, which is crucial for enhancing the performance of neuromorphic circuits. Similarly, a broader NDTR defines the width of the intermediate logic states in ternary inverter applications. Furthermore, our study shows that adjusting iodine (I^-) concentration allows for ion-enabled reconfigurability, facilitating seamless transitions between binary and ternary logic circuit operations. Our findings highlight the importance of fine-tuning device parameters to achieve robust and tunable NDT behavior, underscoring the potential of the OECTs for next-generation electronic and neuromorphic applications.

2. Results and Discussion

A comprehensive overview of the structural, material, and operational aspects of the N-shaped OECTs is displayed in **Figure 1**. More in detail, in Figure 1a, a schematic of the device architecture is shown, highlighting the planar configuration where the gate, source, and drain electrodes are co-planar on a glass substrate. An aqueous KI solution is used as the electrolyte.

Figure 1b depicts the chemical structure of the p(C_4DPP-T) polymer, employed as the active semiconducting layer. This polymer functions as a p-type semiconductor, enabling hole transport. The highest occupied molecular orbital (HOMO) energy level of p(C_4DPP-T) was determined by photoelectron spectroscopy in air (PESA) to be –4.8 eV (Figure S1, Supporting Information), indicating suitable alignment for efficient hole injection and transport. Figure S2 (Supporting Information) displays the transfer and output characteristics of p(C_4DPP-T)-based OECTs with a KCl electrolyte, clearly demonstrating a typical, monotonic current–voltage behavior due to hole accumulation. Figure 1c presents the atomic force microscopy (AFM) image (1 μm × 1 μm) illustrating the surface morphology of the p(C_4DPP-T) films. The image reveals a smooth surface with a roughness of ≈1 nm, which is favorable for uninterrupted transport of the charge carriers.

Figure 1d presents the device configuration for operational mode 1, where the V_{DS} was fixed at −0.3 V, the source terminal was grounded (V_S = 0 V), and V_{GS} was swept from 0 to −0.65 V. The resulting transfer curve, shown in Figure 1e, exhibits four distinct operational regions: 1) Range I (0 < V_{GS} < −0.2 V), where the device remains in the off state; 2) Range II (−0.2 V < V_{GS} < −0.29 V), where I_{DS} increases with V_{GS}, reaching a peak current (I_P) of 2 μA at a peak voltage (V_P) of −0.29 V; 3) Range III (−0.29 V < V_{GS} < −0.45 V), where NDT is observed, as I_{DS} decreases from 2 μA to a valley current (I_V) of 1.4 μA at V_V = −0.45 V. This range yields a PVR (= I_P /I_V) of 1.4 and an NDTR (= |V_V - V_P|) of 0.16 V; and 4) Range IV (V_{GS} > −0.45 V), where I_{DS} shows a second current enhancement from 1.4 to 3.2 μA at V_{GS} = −0.65 V. This sequence gives rise to the distinctive N-shaped transfer curve, with a maximum negative transconductance (g_m) of −6.7 μS at V_{GS} = −0.36 V, as shown in Figure 1f. For clarity, the extracted metrics for Mode 1 are summarized in **Table 1**. The performance metrics across six OECTs are summarized in Figure S3 (Supporting Information), where the average NDTR and PVR were estimated to be 0.17 ± 0.05 V and 1.5 ± 0.2, respectively. The stability and repeatability of the N-shaped transfer characteristics were also examined. As shown in Figure S4 (Supporting Information), the device exhibits a small but distinct hysteresis between the forward and reverse V_{GS} sweeps. Nevertheless, the forward scans show excellent stability, as confirmed by the repetitive cycling measurements in Figure S5 (Supporting Information), where 20 consecutive V_{GS} sweeps display negligible variation in the current amplitude or peak position, indicating the absence of degradation or irreversible electrochemical changes. Long-term stability tests

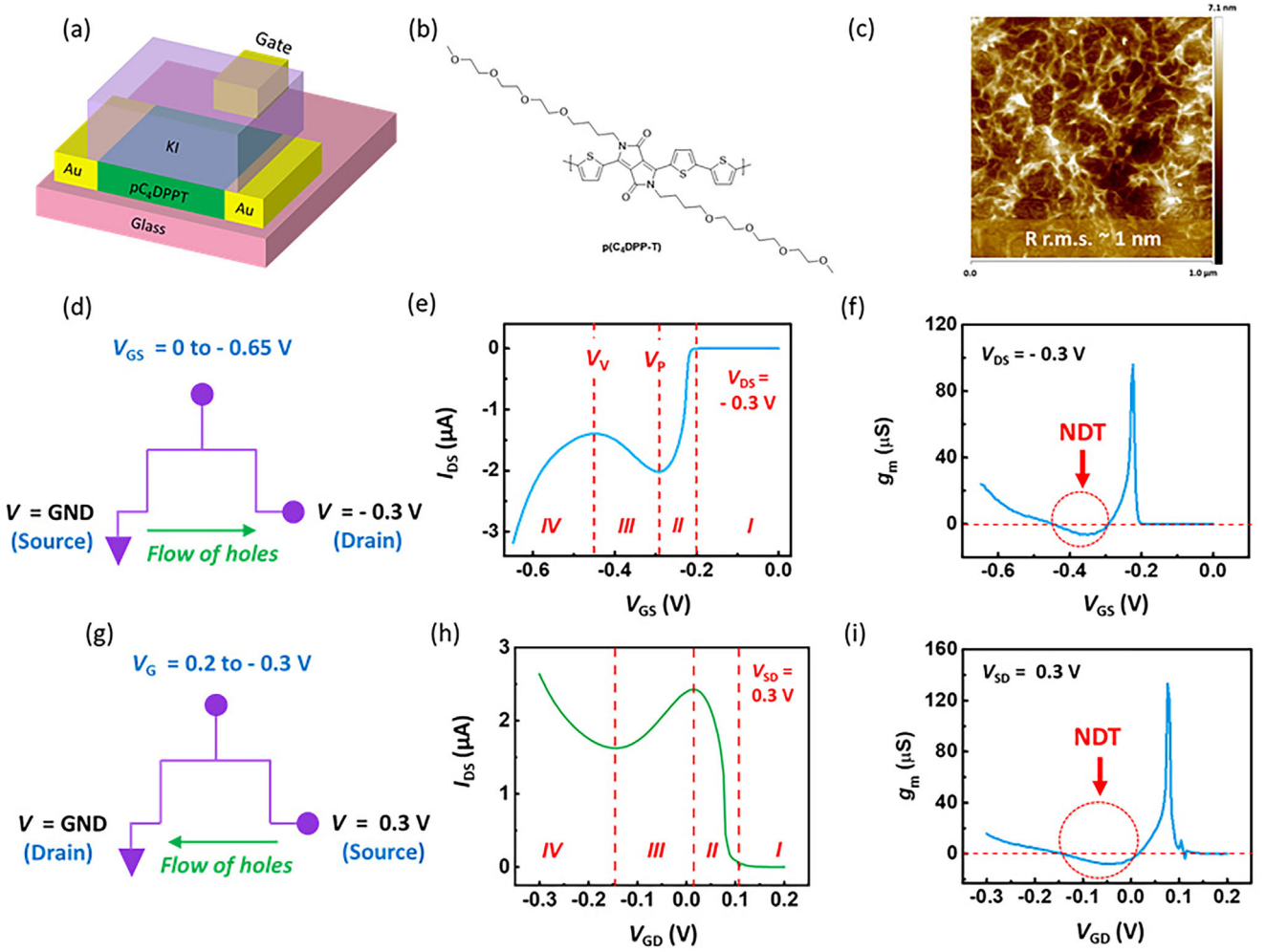

Figure 1. a) Schematic of the OECT architecture. b) Chemical structure of the p(C_4DPP-T) polymer. c) AFM image showcasing the surface morphology of the p(C_4DPP-T) film. d) Circuit configuration for operational mode 1. e) Transfer characteristics of the OECTs at $V_{DS} = -0.3$ V. f) Variation of transconductance as a function of V_{GS} at $V_{DS} = -0.3$ V g) Circuit configuration for operational mode 2 h) Transfer characteristics of the OECTs at $V_{SD} = 0.3$ V i) Variation of transconductance as a function of V_{GD} at $V_{SD} = 0.3$ V.

(Figure S6, Supporting Information) reveal that the characteristic NDT response remains stable even after 12 and 48 days of storage in ambient air, with NDTR and PVR values of 0.20 ± 0.02 V and 2.1 ± 0.4, respectively. These results confirm that the electrical response of the devices is robust and reproducible, showing negligible degradation under cyclic operation and long-term ambient storage.

Figure 1g presents the second OECT operational mode (mode 2), in which a positive voltage is applied to one electrode, functioning as the source ($V_{SD} = 0.3$ V), while the other electrode, grounded, acts as the drain (V_D = GND) and the gate voltage (V_{GD}) is swept from 0.2 to −0.3 V. A similar N-shaped behavior is observed as shown in Figure 1h, but with I_{DS} showing positive values due to the reversed flow of holes as indicated in Figure 1d,g. The peak-to-valley characteristics in this mode are as follows: $V_P = 0.01$ V, $V_V = -0.15$ V, NDTR = 0.16 V, $I_P = 2.4$ μA, $I_V = 1.6$ μA and PVR = 1.5. The maximum g_m in this mode is −8.2 μS at $V_{GD} = -0.04$ V as shown in Figure 1i. The corresponding metrics for Mode 2 are also included in Table 1. The V_{SD}-dependent NDT behavior of the OECTs is presented in Figure S7 (Supporting Information).

From these observations, it is evident that the N-shape behavior is governed by the voltage difference between the drain and gate voltage. For instance, the I_{DS} peaks when $|V_{DS} - V_{GS}| = 0.01$ V in mode 1, and $|V_D - V_{GD}| = 0.01$ V in mode 2. Notably, the second operational mode reduces the required gate voltage to attain the N-shaped curve by ≈50%, requiring a maximum gate amplitude of 0.3 V, compared to 0.65 V in mode 1.

Table 1. Summary of key performance metrics for OECTs in operational modes 1 and 2.

Operation	V_P [V]	V_V [V]	NDTR [V]	I_P [μA]	I_V [μA]	PVR	g_m [μS]
Mode 1	−0.29	−0.45	0.16	2	1.4	1.4	− 6.7
Mode 2	0.01	−0.15	0.16	2.4	1.6	1.5	− 8.2

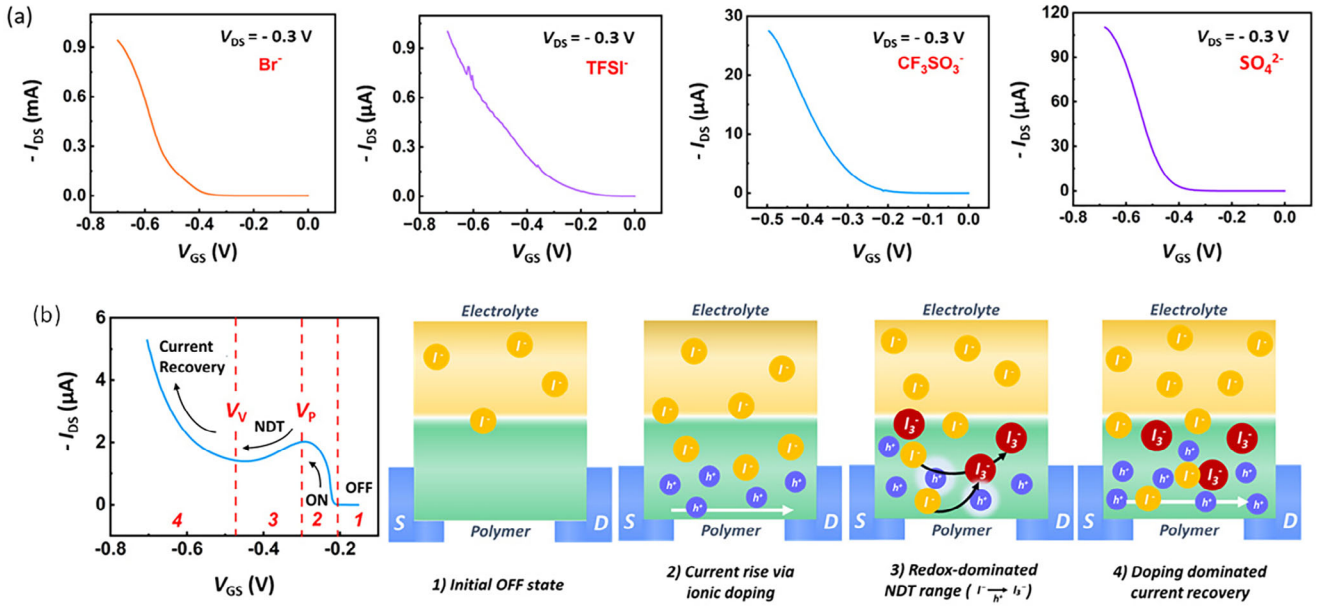

Figure 2. a) Transfer characteristics of p(C_4DPP-T)-based OECTs operated with different anions: Br^-, $TFSI^-$, $CF_3SO_3^-$, and SO_4^{2-}. b) N-shaped transfer characteristics of the KI-gated OECT, showing distinct peak and valley features. Schematic representations of the proposed mechanism across four operational regimes (1–4).

Figure 2 illustrates the possible physical mechanism underlying the NDT behavior observed in the devices when operated in an aqueous KI electrolyte. Figure 2a presents the transfer characteristics of p(C_4DPP-T)-based OECTs using various other anions. Similar to the behavior of Cl^- (shown in Figure S2, Supporting Information), the halide ion Br^- also exhibits typical p-type characteristics with a monotonic increase in I_{DS}. Additionally, devices using bulkier anions such as $TFSI^-$, $CF_3SO_3^-$, and SO_4^{2-} also display conventional p-type behavior, further highlighting the NDT response observed specifically with KI. The variation in current magnitude across different anions likely arises from differences in ionic size, hydration, and polymer–ion affinity, which influence ion desolvation and penetration into the channel.[41,42] In contrast, KI-based devices exhibit a pronounced N-shaped transfer curve (Figure 2b) with four operational regimes, which is attributed to the formation of triiodide species and a redox-mediated modulation of ionic doping dynamics.[43–46] This interpretation is supported by complementary electrochemical and spectroscopic analyses, including UV–vis absorption of electrochemically doped films, X-ray photoelectron spectroscopy (XPS), cyclic voltammetry, starch–iodine test, and H_3PO_2 reduction test, and is consistent with prior literature reports involving triiodide formation and iodine redox chemistry.[43–46]

The proposed mechanism is outlined below, with schematic representations shown in Figure 2b (stages 1–4): 1) Initial Off-State: At low V_{GS}, the migration of I^- ions toward the polymer is negligible, leading to minimal ionic doping of the p(C_4DPP-T) channel. As a result, the hole density remains low, and the device operates in the off state. 2) Current Rise via Ionic Doping: As V_{GS} becomes more negative, I^- ions migrate toward the polymer leading to enhanced doping and a gradual increase in I_{DS}. This marks the transition from the off state to the conductive regime. In this range, the optical spectra remain unchanged (Figure S8, Supporting Information), indicating that the process is dominated by ionic doping rather than redox activity. 3) NDT range: As V_{GS} is further increased, redox interactions between the polymer and iodide ions become dominant, leading to the oxidation of I^- to triiodide (I_3^-). The holes present in the polymer facilitate this redox reaction, participating in the oxidation of I^- and being progressively consumed to yield I_3^- via the following pathways: (i) $2I^- + 2\,h$ (hole polaron) $\rightarrow I_2$ followed by $I_2 + I^- \leftrightarrow I_3^-$.[43–45] The formation of I_3^- is directly confirmed by the UV–vis absorption spectroscopy of electrochemically doped films (Figure S8, Supporting Information), which shows a distinct growth of the characteristic I_3^- band at 372–390 nm as the applied doping potential increases.[47] X-ray photoelectron spectroscopy (XPS) was further conducted to validate the presence of I_3^- species (Figure S9, Supporting Information). The doped film exhibits two distinct iodine peaks at 618.9 eV (I $3d_{5/2}$) and 630.4 eV (I $3d_{3/2}$), characteristic of the I_3^- doublet.[48] The absence of these peaks in the pristine film and their appearance after electrochemical doping confirm the formation and surface accumulation of I_3^- species. This surface enrichment is also accompanied by an increase in surface roughness in the AFM image (Figure S10, Supporting Information), suggesting physical accumulation of I_3^- at the polymer surface. In this regime, hole consumption associated with the redox conversion becomes the dominant process, resulting in a substantial reduction in hole population within the channel and thus a decrease in I_{DS}, which manifests as the NDT region. Additional experiments corroborate this redox-driven mechanism. Figure S11 (Supporting Information) supports this redox process by showing the cyclic voltammetry (CV) of the p(C_4DPP-T)/KI system. Simultaneously, a visible color change is observed during CV scans, indicating redox activity consistent with I_3^- generation. Additionally, a qualitative starch–iodine test (Figure S12, Supporting Information) revealed

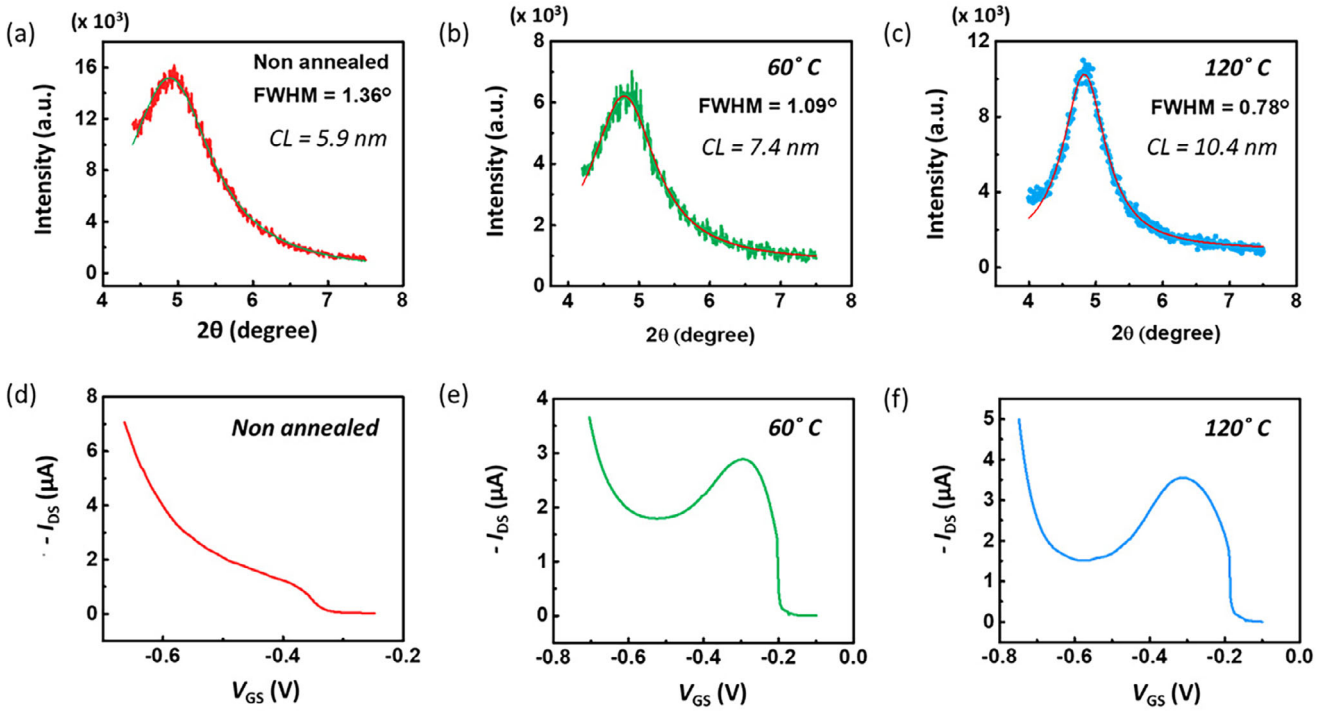

Figure 3. XRD patterns of p(C_4DPP-T) films processed under different annealing conditions: a) non-annealed, b) annealed at 60 °C for 15 min, and c) annealed at 120 °C for 15 min. Peak fitting was used to extract the full width at half maximum (FWHM) and calculate the coherence length (CL). d–f) Transfer characteristics of OECTs based on p(C_4DPP-T) films, corresponding to the same annealing conditions as in (a–c), respectively.

a distinct color change from green to dark blue upon starch addition, consistent with the formation of a [I_3^-·starch] complex.[49] The presence of I_3^- ions is also supported by Figure S13 (Supporting Information), where qualitative hypophosphorous acid (H_3PO_2) reduction test was performed. Upon the addition of H_3PO_2, the dark brown color changes to green color, confirming the chemical reduction of I_3^- back to I^-.[50] This color change also supports the presence of I_3^- in the channel environment. 4) Recovery of Current: At larger negative V_{GS}, the I_{DS} begins to recover, indicating that the system regains its doping ability. This recovery is correlated with the saturation of the optical absorption associated with I_3^- (Figure S8, Supporting Information), indicating that the redox conversion has reached a steady state. Once the formation of I_3^- species ceases to progress, the strongly negative V_{GS} provides sufficient driving force for I^- ions to penetrate the polymer channel, re-establishing effective hole doping. Consequently, the device transitions back to a doping-dominated regime completing the N-shaped transfer behavior. Overall, the device operation proceeds through three distinct regimes: an initial doping phase, a redox-dominated NDT phase, and a final re-doping phase that collectively give rise to the characteristic N-shaped response.

Beyond these chemical and spectroscopic signatures, the structural, mass, and electrochemical characteristics were further examined by X-ray diffraction (XRD), electrochemical quartz crystal microbalance (EQCM) and I_{GS}–V_{GS} measurements (Figures S14–S16, Supporting Information). The XRD patterns show a reversible suppression of the diffraction peak at 0.6 V, indicating a transient loss of polymer order during redox and its recovery upon dedoping. This structural modulation coincides with the pronounced frequency drop observed in the EQCM data beyond 0.5 V, signifying concurrent mass uptake by ion and solvent ingress into the polymer matrix. Consistently, the KI-gated devices exhibit gate currents several orders of magnitude higher than those using other anions, evidencing Faradaic charge-transfer processes rather than purely capacitive behavior.[51] Collectively, these results further confirm that the iodide-driven NDT originates from a reversible redox process.

To evaluate the universality of this iodide-mediated mechanism, additional OECTs based on other polymers were examined. While PEDOT:PSS devices showed conventional monotonic behavior (Figure S17, Supporting Information), accumulation-mode OECTs with polymers such as pgBTTT and p(g3T2-T) also exhibited N-shaped transfer characteristics (Figures S18, Supporting Information), confirming that the iodine-driven NDT behavior is not limited to p(C_4DPP-T) but can be generalized to other p-type accumulation-mode systems.

Having established the iodide-mediated NDT mechanism and its generality across multiple polymers, we next investigated how the polymer microstructure influences its characteristics (**Figure 3**). Since ionic transport and redox activity are closely related to chain packing and interfacial order, p(C_4DPP-T) films were processed under three conditions: non-annealed, annealed at 60 °C, and annealed at 120 °C.[52,53] The corresponding XRD patterns are shown in Figure 3a–c. The full width at half maximum (FWHM) was extracted via peak fitting and used to calculate the coherence length (CL) using the equation: $CL = K \bullet \lambda / \beta \bullet \cos\theta$, where K is the Scherrer constant, λ is the X-ray wavelength, β is the FWHM in radians, and θ is the Bragg angle. The results indicate that the coherence length increased

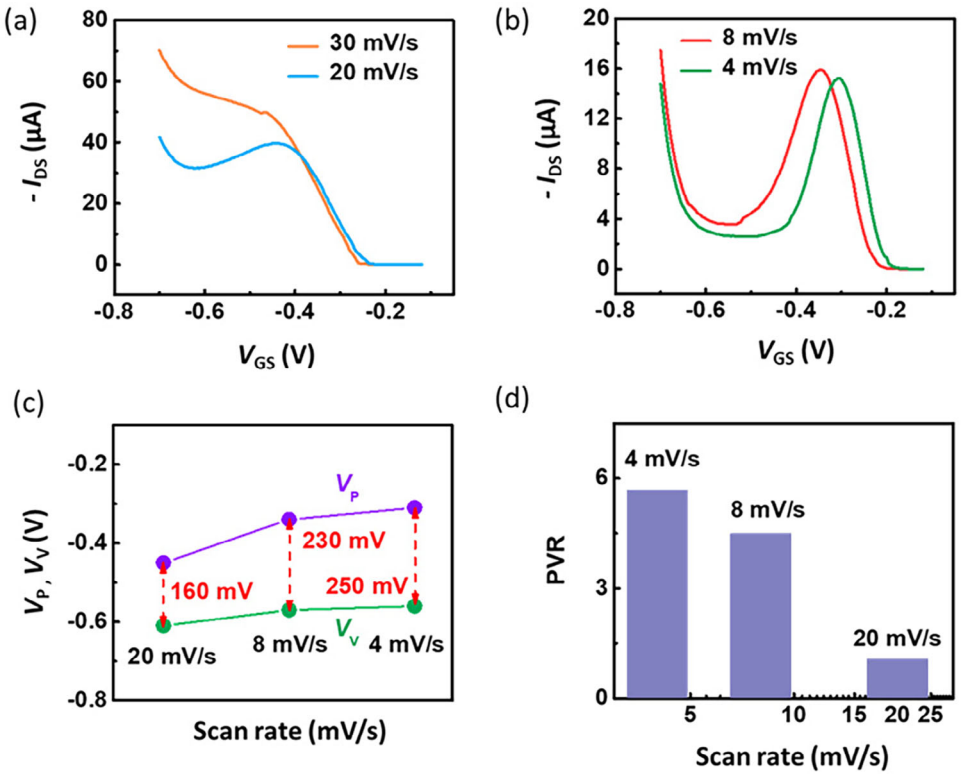

Figure 4. a) Transfer characteristics of the OECT at a V_{GS} scan rate of 30 and 20 mV s^{-1}. b) Transfer characteristics at V_{GS} scan rates of 8 and 4 mV s^{-1}. c) Variation of V_P and V_V as a function of scan rate. d) Variation of PVR as a function of scan rate.

gradually from 5.9 nm in the non-annealed films to 10.4 nm in the films annealed at 120 °C, suggesting that annealing promotes greater crystallinity in the films.

The impact of microstructure on device operation is evident in the transfer characteristics shown in Figure 3d–f. In the non-annealed condition, the device shows a monotonic current response without NDT behavior. Upon annealing at 60 °C, an N-shaped transfer curve appears with a PVR of ≈1.6. At 120 °C, the NDT becomes more pronounced, with a PVR of ≈2.5 and a well-defined current drop. This crystallinity-dependent evolution supports the redox-mediated mechanism. In less crystalline films, the loosely packed structure allows ions to diffuse deeply into the bulk, resulting in spatially distributed redox and doping processes that yield a weaker NDT response. In contrast, in highly crystalline films, the denser molecular packing constrains ion transport and promotes a more localized and cooperative redox process near the ordered domains, giving rise to a sharper NDT and higher PVR.[52,53]

The pronounced N-shaped response in p(C_4DPP-T) therefore originates from its intrinsically favorable electronic and structural attributes. The close alignment between its HOMO (–4.8 eV) and the iodide/iodine redox potential (–4.98 eV) enables efficient charge exchange, while its ordered structure provides a confined redox activity. Together, these characteristics facilitate the redox-driven modulation of hole transport that gives rise to the well-defined NDT behavior observed in this polymer.

We next examined how device geometry influences its electrical characteristics. The effect of the channel width-to-length ratio (W/L) was studied while keeping the annealing condition fixed at 60 °C, as shown in Figure S19 (Supporting Information). Increasing the channel width-to-length ratio (W/L ratio) resulted in a substantial improvement in the overall I_{DS}, with I_P increased significantly from 3 to 120 μA for W/L ratio changed from 0.25 to 10.

Following our study on the effects of p(C_4DPP-T) polymer processing conditions and device geometry, we explored the influence of V_{GS} scan rate on the NDT behavior while keeping V_{DS} fixed at −0.3 V and W/L ratio at 10 (**Figure 4**). The scan rate is critical as it determines the operational speed of the device and also controls the time scale of the polymer-iodide interactions and doping dynamics. To investigate its impact, we gradually reduced the scan rate from 30 to 4 mV s^{-1}. The resulting transfer characteristics are presented in Figure 4a,b. At the highest scan rate of 30 mV s^{-1}, no NDT behavior was observed. However, reducing the scan rate to 20 mV s^{-1} resulted in a small but noticeable NDT, which became significantly pronounced at a scan rate of 8 mV s^{-1}, displaying a distinct peak and valley in the I_{DS} response. This behavior approached saturation at 4 mV s^{-1}, indicating a limit to the enhancement achievable through further reduction of the scan rate.

To quantify these observations, Figure 4c presents the variation of V_P and V_V as a function of the scan rate. Notably, V_P shifted significantly from −0.45 V at 20 mV s^{-1} to −0.34 V at 8 mV s^{-1}, with only a slight further shift to −0.31 V at 4 mV s^{-1}. In contrast, V_V exhibited minimal shifts, moving by only 0.04 V from 20 to 8 mV s^{-1} and by an additional 0.01 V at 4 mV s^{-1}.

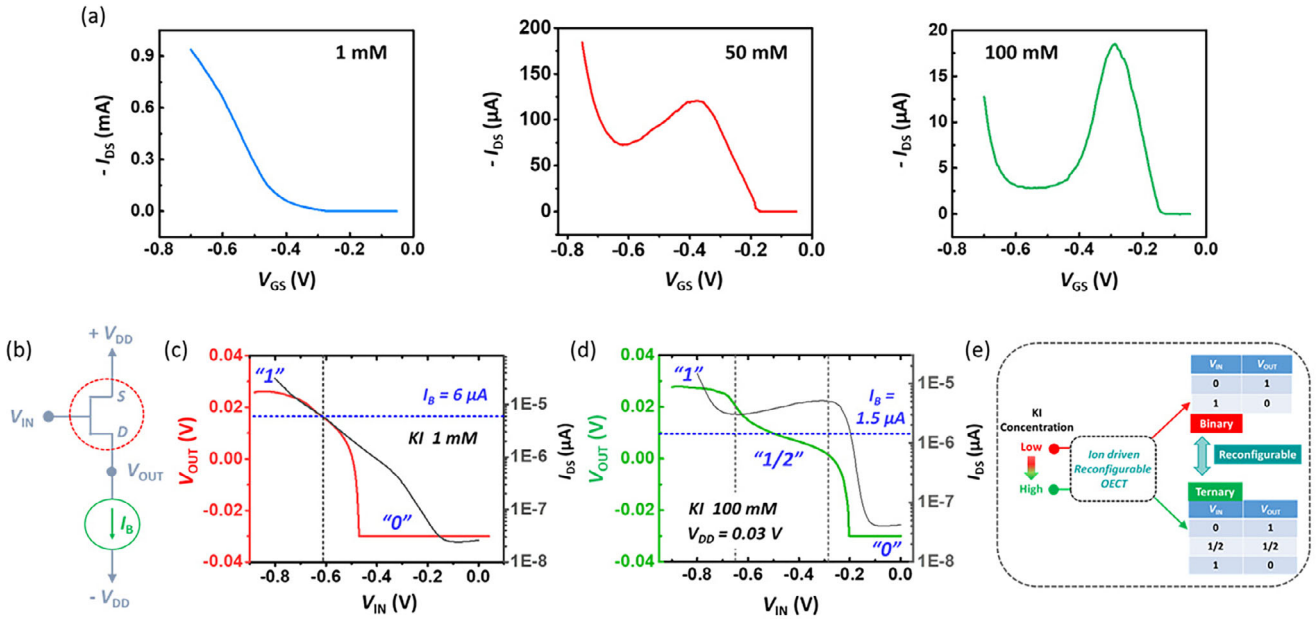

Figure 5. a) Transfer characteristics of OECTs at KI concentrations of 1, 50, and 100 mM. b) Circuit schematic of the current-driven OECT. c) Voltage transfer characteristics (VTC, red line) of the circuit at a KI concentration of 1 mM along with the transfer characteristics (black line) of the OECT without a current source. d) VTC of the circuit at a KI concentration of 100 mM, along with the corresponding OECT characteristics without a current source. e) Illustration of ion-driven reconfigurability, demonstrating logic state transitions based on electrolyte concentration.

Consequently, the NDTR expanded from 160 mV at 20 mV s^{-1} to 230 mV at 8 mV s^{-1}, and then to 250 mV at 4 mV s^{-1}. This behavior highlights the time-dependent nature of ionic migration and polymer–iodide redox dynamics. At fast scans, I^- ions lack sufficient time to migrate and undergo efficient oxidation to I_3^-, requiring more negative V_{GS} to trigger these processes. At slower scans, ions can gradually accumulate and participate in hole-assisted redox conversion, leading to earlier NDT onset (less negative V_P).

The PVR of the OECTs was also extracted as a function of scan rate, as shown in Figure 4d. The PVR improved significantly from 1.1 at 20 mV s^{-1} to 4.5 at 8 mV s^{-1}, with a further slight increase to 5.7 at 4 mV s^{-1}. This indicates that lowering the scan rate not only enhances NDTR but also significantly improves the PVR. The improvement arises from the extended interaction time between the polymer and electrolyte at slower scans, which enables more complete ionic doping at low bias and more efficient hole consumption through redox conversion. The slow sweep of V_{GS} allows iodide ions sufficient time to migrate and accumulate within the active region, promoting earlier and stronger doping of the polymer channel. For example, I_{DS} at V_{GS} = – 0.24 V increases from ≈0.8 μA (20 mV s^{-1}) to ≈1.7 μA (8 mV s^{-1}) and ≈6 μA (4 mV s^{-1}), reflecting enhanced doping kinetics at lower scan rates. Meanwhile, the longer dwell time per voltage step facilitates more complete oxidation of I^- to I_3^-, resulting in greater hole consumption and a more pronounced current reduction in the NDT region. Together, these time-dependent ionic and redox processes yield a deeper and sharper NDT feature, confirming that the NDT strength and PVR are determined by the kinetic balance among ionic migration, redox conversion, and hole transport in the polymer.

Next, we varied the concentration of the KI electrolyte from 1 to 100 mM to explore its impact on NDT behavior (**Figure 5**). Figure 5a shows the corresponding transfer characteristics of the OECTs. At 1 mM KI, the device exhibits a typical monotonic p-type response with no NDT feature, owing to the limited iodide availability and the absence of noticeable redox activity. Increasing the concentration to 50 mM induces a clear N-shaped response, indicating the onset of redox-mediated modulation of channel conductivity enabled by enhanced iodide accumulation. Further increasing the concentration to 100 mM results in a more pronounced NDT feature with a sharper peak–valley profile. Quantitatively, V_P shifts from –0.38 V at 50 mM to –0.29 V at 100 mM, while V_V shifts slightly from –0.14 to –0.10 V, expanding the NDTR from 240 to 290 mV. The PVR rises sharply from 1.6 at 50 mM to 6.6 at 100 mM, demonstrating that higher ionic strength strongly amplifies the NDT response. The obtained NDTR and PVR values are notably high and highly competitive among reported NDT-type transistors. For comparison, we have included Table S1 (Supporting Information), summarizing NDTR and PVR values from representative OECT and OFET systems.[28,29,31,32,38–40]

This enhancement stems from the greater supply of mobile iodide ions, which strengthens the electrochemical coupling between the electrolyte and the polymer. At low concentrations, the limited iodide flux restricts hole doping, resulting in a monotonic current increase. As the concentration rises, ionic doping becomes more efficient, and the current at low bias increases markedly, for instance, I_{DS} at V_{GS} = –0.18 V grows from ≈19 nA (1 mM) to ≈1.7 μA (50 mM) and ≈4.2 μA (100 mM). However, despite this stronger doping at high ionic strength, the peak current (I_P) at 100 mM is lower than that at 50 mM. This reduction arises

because the higher iodide concentration accelerates the onset of redox conversion, causing earlier hole consumption and limiting the maximum achievable current before the NDT region. Once the polymer becomes sufficiently doped, the accumulated holes drive the oxidation of I^- to I_3^-, progressively depleting hole density and suppressing the channel current. The stronger competition between hole generation and hole consumption at higher iodide concentrations therefore, produces a lower I_P, a sharper current drop, and a well-defined N-shaped transfer curve. Overall, the evolution of NDT behavior with KI concentration reflects a delicate kinetic interplay among ionic transport, charge transfer, and redox chemistry within the polymer. This interpretation is further supported by CV measurements (Figure S20, Supporting Information), showing negligible redox activity at 1 mM KI and a distinct anodic–cathodic response at 50 mM, accompanied by a visible color change from green to brown, confirming the enhanced I^- to I_3^- conversion at higher concentrations.

This concentration-dependent trend closely mirrors the scan-rate-dependent behavior. In both cases, conditions that promote greater iodide availability and sufficient interaction time favor more efficient I^- to I_3^- conversion, leading to an earlier NDT onset (less negative V_P) and a higher PVR. The absence of NDT at 1 mM KI further indicates that a critical iodide concentration is required to activate the redox process and generate measurable modulation of channel conductivity.

In support of this interpretation, non-annealed p(C_4DPP-T) OECTs that did not exhibit NDT at 50 mM KI were found to display clear NDT behavior at 500 mM KI (Figure S21, Supporting Information). This observation confirms that even in less-ordered films, sufficiently high ionic strength can activate the iodide redox process and trigger NDT behavior, highlighting the critical role of electrolyte concentration in governing redox-driven NDT dynamics.

These results demonstrate that increasing KI concentration is another effective way to enhance the NDT behavior and PVR of OECTs, making concentration tuning a valuable tool for optimizing device performance. Moreover, the impact of the ion concentration on the electrical characteristics (Figure 5a) suggests that p(C_4DPP-T)-based OECTs offer a significant degree of reconfigurability as a function of I^- concentration. For low I^- concentrations, the device operates as a typical OECT, while for higher I^- concentrations, nonlinear characteristics emerge, enabling the device to provide different logic states on the fly.

To demonstrate the concept of "ion-enabled reconfigurability,", we constructed and examined reconfigurable logic circuits. Figure 5b–e demonstrates that iodine (I^-) concentration effectively facilitates reconfigurability in OECT-based circuits, enabling transitions between binary and ternary logic operations. The current-driven OECT configuration is illustrated in Figure 5b. In this circuit, the OECT is connected in series with a current generator, resembling an inverter topology.[54] The input voltage (V_{IN}) is applied to the gate ($V_G = V_{IN}$), and the output voltage (V_{OUT}) is measured at the drain terminal ($V_D = V_{OUT}$). The bias current (I_B) is established by the current generator, and the topology ensures that the current at drain/output terminal is set to $I_{OUT} = I_B$. In this circuit, the OECT functions as a driver, while the current generator acts as a zero-V_{GS} load. Unlike conventional CMOS inverters that rely on complementary p-n transistors, this circuit serves as a proof-of-concept architecture that leverages the N-shaped antiambipolar transfer characteristics of the OECT to demonstrate ion-driven reconfigurable logic operation.

Figure 5c shows the voltage transfer characteristics (red line) of the current-driven OECT for a low KI concentration (1 mM) along with the corresponding transfer characteristics (black line) of the OECT. The OECT circuit demonstrates conventional binary logic with two distinct states:

1) Logic 1: at large and negative V_{IN} the OECT is in the on state, resulting in low channel resistance (R_o). V_{OUT} of the circuit is given by $V_{OUT} = V_{DD} - I_B \times R_o$. Since R_o is low, $V_{OUT} \approx V_{DD}$.
2) Logic 0: The OECT transitions from the on state to the off state due to low negative V_{IN}, resulting in high R_o. Since R_o is high, $V_{OUT} \approx -V_{DD}$.

Interestingly, Figure 5d shows that at a higher KI concentration of 100 mM, the OECT exhibits NDT characteristics, enabling ternary logic circuit operation with three logic states:

1) Logic 1: At large and negative, V_G the OECT is in the on state, the channel resistance R_o is small, and $V_{OUT} \approx V_{DD}$.
2) Logic ½: The OECT is partially on in the NDT range, and $V_{OUT} \approx 0$ V to sustain $I_B = 1.5$ µA at the output terminal.
3) Logic 0: At small V_G, the OECT channel resistance is large and hence $V_{OUT} \approx -V_{DD}$.

The ternary circuit operation was further verified through consecutive voltage sweeps and I_B-dependent measurements, and was additionally examined at a higher V_{DD} of 0.3 V (Figure S22, Supporting Information), confirming stable operation with tunable intermediate states and sharper voltage transitions at elevated supply voltage.

Figure 5e presents a schematic of ion-driven reconfigurability in the nonlinear OECT circuit, enabling transitions between binary and ternary logic states based on KI concentration (low or high). Such ion concentration-driven dynamic reconfigurability between binary and ternary logic states highlights the potential of these unique N-shaped OECT-based circuits for applications requiring adaptable logic operations. This feature is valuable for multivalued logic (with more than two logic states), improving computing efficiency, and decision-making systems, where the circuit adapts to extreme conditions by switching logic states.[2,55,56] It is also applicable in real-time adaptive systems like environmental and biological sensing and neuromorphic computing.[57,58]

To further explore the relevance of the NDT OECTs, we have also fabricated a current-driven circuit using a BBL-based OECT, with its voltage transfer characteristics shown in Figure S23 (Supporting Information). BBL-based OECTs are commonly known for their "Λ"-shaped behavior. However, such antiambipolar behavior does not exhibit the second current enhancement range, as observed in N-shaped behavior, which limits its ability to support full-swing ternary logic circuits.

3. Conclusion

In conclusion, we demonstrated unique N-shaped NDT behavior in OECTs using the combination of p(C_4DPP-T) polymer and KI electrolyte. This behavior is attributed to a doping/redox/doping

mechanism, where the initial rise in I_{DS} originates from I^--induced doping, followed by a current drop due to redox-driven hole consumption through I^- to I_3^- conversion, and a final current increase resulting from renewed doping at higher negative V_{GS}. To optimize the NDT response, we systematically varied polymer-annealing conditions, KI concentration, and V_{GS} scan rate. Optimized annealing enhanced the PVR, while a minimum iodide concentration and slower scan rates were essential to trigger and sharpen the NDT effect. By fine-tuning these parameters, we achieved an NDTR of 290 mV and a PVR as high as 6.6, underscoring the importance of precise control over device parameters to enable tunable and optimized NDT behavior. Moreover, we demonstrated iodine ion (I^-) concentration-driven reconfigurability in OECT-based circuits, facilitating transitions between binary and ternary logic states. As ion concentration increases, the circuit behavior shifts from binary to ternary logic, underscoring the reconfigurability of the device, which can enable electrolyte-dependent logic and decision-making. Our findings, therefore, highlight the potential of "N"-shaped NDT-OECTs for advanced electronic applications, including reconfigurable and multivalued logic circuits and neuromorphic devices.

4. Experimental Section

The OECTs were fabricated on standard microscope glass slides (75 mm × 25 mm), which were thoroughly cleaned in an ultrasonic bath prior to fabrication. The cleaning procedure involved an initial wash with a Micro-90 soap solution, followed by rinsing in a 1:1 volume mixture of acetone and isopropanol. After cleaning, gold source, drain, and gate electrodes were photolithographically patterned onto the slides using positive Microposit S1813 photoresist.

Two layers of parylene C were then deposited. To facilitate separation between the layers, a soap solution (1% vol/vol Micro-90 in deionized water) was applied between the parylene C layers. This enabled peeling off the upper layer of parylene C, while the lower layer served as insulation for the gold electrodes. A silane adhesion promoter (γ-methacryloxypropyl trimethoxysilane, A-174) was used while depositing the lower parylene C layer to enhance adhesion.

In the second photolithography step, using positive photoresist AZ 9260, the transistor channels were defined. The transistor channels were fixed with two distinct dimensions: $W_1 \times L_1 = 25\ \mu m \times 100\ \mu m$ and $W_2 \times L_2 = 200\ \mu m \times 20\ \mu m$. Reactive ion etching (160 W O_2/CF_4 plasma for 16 min, with an O_2 flow rate of 50 sccm and CHF_3 flow rate of 5 sccm) was employed to etch the channels through the photoresist mask. A 90 nm-thick p(C_4DPP-T) film was subsequently deposited by spin-coating from a chloroform solution at 1000 rpm for 45 s, followed by an initial annealing step at 60 °C for 1 min. After the second parylene C layer was peeled off, the polymer underwent an additional annealing process at 60 °C for 15 min.

To investigate the influence of annealing conditions, three distinct protocols were used: 1) No annealing applied after spin coating, 2) an initial annealing at 60 °C for 1 min followed by 15 min after peeling off the parylene layer, and 3) a higher temperature annealing at 120 °C for 1 min prior to peel-off, followed by 15 min at the same temperature post-peel-off.

The electrical characterization of the OECTs, specifically current–voltage measurements, was conducted using a Keithley 2400 semiconductor parameter analyzer.

CV measurements were performed in an ambient air atmosphere using an Autolab PGSTAT101 with a three-electrode setup. The measurements were performed in an aqueous 100 mM KI electrolyte at a scan rate of 10 mV s^{-1}, with Ag/AgCl aqueous reference electrode (BAS, RE-1B), and Pt mesh as the counter electrode, and polymers were spin-coated on an ITO substrate as the working electrode.

Acknowledegements

The authors acknowledge the Alexander von Humboldt Foundation for funding this research, including financial support for materials and experimental resources. The authors also acknowledge Helma Burg and Rüdiger Berger from the Atomic Force Microscopy Core Facility for their contributions to Atomic Force Microscopy measurements and Leon Prädel for performing the XPS measurements. Additionally, the authors thank Michelle Beuchel, Christian Bauer, and Sirma Koynova for their technical support. Moreover, the authors sincerely thank Dr. Renan Colucci and Hannes Wöffen for their time and support in conducting the EQCM measurements.

Supporting Information

Supporting Information is available from the Wiley Online Library or from the author.

Conflict of Interest

The authors declare no conflict of interest.

Data Availability Statement

The data that support the findings of this study are available from the corresponding author upon reasonable request.

Keywords

antiambipolar transistor, ion-driven reconfigurability, negative differential transconductance, organic electrochemical transistor, reconfigurable Logic

Received: August 28, 2025
Revised: November 25, 2025
Published online:

[1] K. Kobashi, R. Hayakawa, T. Chikyow, Y. Wakayama, *Adv. Electron. Mater.* **2017**, *3*, 1700106.
[2] Y. Wakayama, C. H. Kim, D. Panigrahi, R. Hayakawa, *Mater. Adv.* **2022**, *3*, 5260.
[3] Y. Meng, W. Wang, W. Wang, B. Li, Y. Zhang, J. Ho, *Adv. Mater.* **2024**, *36*, 2306290.
[4] J. Liu, J. Liu, J. Zhang, C. Li, Q. Cui, F. Teng, H. Li, L. Jiang, *J. Mater. Chem. C* **2020**, *8*, 4303.
[5] J. Zhu, T. Mori, *Adv. Electron. Mater.* **2023**, *9*, 2200783.
[6] Z. Laswick, X. Wu, A. Surendran, Z. Zhou, X. Ji, G. M. Matrone, W. L. Leong, J. Rivnay, *Nat. Commun.* **2024**, *15*, 6309.
[7] K. G. Cho, D. Z. Adrahtas, K. H. Lee, C. D. Frisbie, *Adv. Funct. Mater.* **2023**, *33*, 2303700.
[8] J. Song, Y. Han, R. H. Koo, J. Seo, H. Yoo, W. Shin, *Small* **2025**, *21*, 2570193.
[9] R. Hayakawa, Y. Yamamoto, K. Yoshikawa, Y. Yamada, Y. Wakayama, *J. Mater. Chem. C* **2025**, *13*, 14234.
[10] K. Kobashi, R. Hayakawa, T. Chikyow, Y. Wakayama, *Nano Lett.* **2018**, *18*, 4355.

[11] D. Panigrahi, R. Hayakawa, K. Fuchii, Y. Yamada, Y. Wakayama, *Adv. Electron. Mater.* **2020**, *7*, 2000940.
[12] R. Hayakawa, K. Honma, S. Nakaharai, K. Kanai, Y. Wakayama, *Adv. Mater.* **2022**, *34*, 2270118.
[13] R. Hayakawa, K. Takahashi, X. Zhong, K. Honma, D. Panigrahi, J. Aimi, K. Kanai, Y. Wakayama, *Nano Lett.* **2023**, *23*, 8339.
[14] X. Hu, J. Meng, T. Feng, T. Wang, H. Zhu, Q. Sun, D. W. Zhang, L. Chen, *Nano Res.* **2024**, *17*, 5614.
[15] B. D. Paulsen, C. D. Frisbie, *J. Phys. Chem. C* **2012**, *116*, 3132.
[16] K. G. Cho, K. H. Lee, C. D. Frisbie, *ACS Appl. Mater. Interfaces* **2024**, *16*, 19309.
[17] X. Wu, Q. He, Z. Zhou, T. L. D. Tam, C. Tang, M. Lin, M. Moser, S. Griggs, A. Marks, S. Chen, J. Xu, I. McCulloch, W. L. Leong, *Adv. Mater.* **2024**, *36*, 2308823.
[18] K. Xu, T. P. Ruoko, M. Shokrani, D. Scheunemann, H. Abdalla, H. D. Sun, C. Y. Yang, Y. Puttisong, N. B. Kolhe, J. S. M. Figueroa, J. O. Pedersen, T. Ederth, W. M. Chen, M. Berggren, S. A. Jenekhe, D. Fazzi, M. Kemerink, S. Fabiano, *Adv. Funct. Mater.* **2022**, *32*, 2112276.
[19] P. C. Harikesh, C. Y. Yang, H. Y. Wu, S. Zhang, M. J. Donahue, A. S. Caravaca, J. D. Huang, P. S. Olofsson, M. Berggren, D. Tu, S. Fabiano, *Nat. Mater.* **2023**, *22*, 242.
[20] P. C. Harikesh, D. Gao, H. Y. Wu, C. Y. Yang, D. Tu, S. Fabiano, *Sci. Adv.* **2025**, *11*, adv3194.
[21] L. Travaglini, K. Fidanovski, D. Mawad, *Adv. Sci.* **2025**, 14448.
[22] W. Chen, H. Jiang, C. Du, Y. Zhong, X. Wang, X. Li, Z. Chen, Q. Liang, F. Sun, Y. Zhu, J. G. Chen, *Adv. Mater.* **2025**, 14904, https://doi.org/10.1002/adma.202514904.
[23] Y. Wang, J. Tang, J. Huang, Q. He, Q. Chen, R. Xie, Y. Zhang, G. Xie, X. Su, X. Wu, *J. Mater. Chem. C* **2025**, https://doi.org/10.1039/D5TC03210E.
[24] R. Granelli, Z. M. Kovács-Vajna, F. Torricelli, *Small* **2025**, *21*, 2410499.
[25] D. K. Tran, S. M. West, A. E. Stewart, W. Kaminsky, S. A. Jenekhe, *Adv. Funct. Mater.* **2025**, 10945, https://doi.org/10.1002/adfm.202510945.
[26] P. C. Harikesh, D. Tu, S. Fabiano, *Nat. Electron.* **2024**, *7*, 525.
[27] H. Yoo, S. On, S. B. Lee, K. Cho, J. J. Kim, *Adv. Mat.* **2019**, *31*, 1808265.
[28] C. Lee, J. Choi, H. Park, C. Lee, C. H. Kim, H. Yoo, S. G. Im, *Small* **2021**, *17*, 2103365.
[29] D. Panigrahi, R. Hayakawa, K. Honma, K. Kanai, Y. Wakayama, *Appl. Phys. Exp.* **2021**, *14*, 081004.
[30] D. Panigrahi, R. Hayakawa, Y. Wakayama, *Adv. Funct. Mat.* **2023**, *33*, 2213899.
[31] J. Choi, C. Lee, C. Lee, H. Park, S. M. Lee, C. H. Kim, H. Yoo, S. G. Im, *Nat. Commun.* **2022**, *13*, 2305.
[32] D. Panigrahi, R. Hayakawa, X. Zhong, J. Aimi, Y. Wakayama, *Nano Lett.* **2023**, *23*, 319.
[33] J. C. Shin, C. Lee, J. Lee, J. Kim, J. A. Jeon, H. Yang, M. Jin, Y. S. Kim, *Small* **2025**, *21*, 2501543.
[34] T. Sarkar, K. Lieberth, A. Pavlou, T. Frank, V. Mailaender, I. McCulloch, P. W. Blom, F. Torricelli, P. Gkoupidenis, *Nat. Electron.* **2022**, *5*, 774.
[35] P. Belleri, J. P. Tarrés, I. McCulloch, P. W. Blom, Z. M. Kovács-Vajna, P. Gkoupidenis, F. Torricelli, *Nat. Commun.* **2024**, *15*, 5350.
[36] J. Seo, S. Kang, D. Kumar, W. Shin, J. Cho, T. Kim, Y. Kim, B. C. Jang, A. R. Trivedi, H. Yoo, *Adv. Funct. Mater.* **2025**, *35*, 2411348.
[37] M. Orlik, *Self-Organization in Electrochemical Systems II*, Springer, Berlin **2012**.
[38] D. Panigrahi, R. Hayakawa, Y. Wakayama, *J. Mater. Chem. C* **2022**, *10*, 5559.
[39] D. Panigrahi, R. Hayakawa, J. Aimi, Y. Wakayama, *Adv. Mater. Technol.* **2023**, *8*, 2301049.
[40] D. H. Tjhe, X. Ren, I. E. Jacobs, G. D'Avino, T. B. Mustafa, T. G. Marsh, L. Zhang, Y. Fu, A. E. Mansour, A. Opitz, Y. Huang, W. Zhu, A. H. Unal, S. Hoek, V. Lemaur, C. Quarti, Q. He, J. K. Lee, I. McCulloch, M. Heeney, N. Koch, C. P. Grey, D. Beljonne, S. Fratini, H. Sirringhaus, *Nat. Mater.* **2024**, *23*, 1712.
[41] C. Cendra, A. Giovannitti, A. Savva, V. Venkatraman, I. McCulloch, A. Salleo, S. Inal, J. Rivnay, *Adv. Funct. Mater.* **2019**, *29*, 1807034.
[42] J. J. Samuel, A. Garudapalli, C. Gangadharappa, S. R. Mahapatra, S. Patil, N. P. B. Aetukuri, *Nat. Commun.* **2022**, *13*, 7788.
[43] A. Turolla, A. Piazzoli, J. F. Budarz, M. R. Wiesner, M. Antonelli, *Chem. Eng. J.* **2015**, *271*, 260.
[44] C. Karunakaran, S. Senthilvelan, S. Karuthapandian, K. Balaraman, *Catal. Commun.* **2004**, *5*, 283.
[45] M. Skunik-Nuckowska, J. Lubera, P. Rączka, A. A. Mroziewicz, S. Dyjak, P. J. Kulesza, *ChemElectroChem* **2022**, *9*, 202101222.
[46] I. Ishita, P. Sahoo, P. K. Sow, R. Singhal, *Electrochim. Acta.* **2023**, *451*, 142286.
[47] S. Moulay, *J. Polym. Eng.* **2013**, *33*, 389.
[48] J. Yu, L. Song, B. Han, J. Hu, Z. Li, J. Mi, *Polymers* **2024**, *16*, 2846.
[49] S. Pesek, M. Lehene, A. M. Brânzanic, R. Silaghi-Dumitrescu, *Molecules* **2022**, *27*, 8974.
[50] S. Park, W. J. Chang, C. W. Lee, S. Park, H. Y. Ahn, K. T. Nam, *Nat. Energy* **2016**, *2*, 16185.
[51] S. T. M. Tan, S. Keene, A. Giovannitti, A. Melianas, M. Moser, I. McCulloch, A. Salleo, *J. Mater. Chem. C.* **2021**, *9*, 12148.
[52] S. H. Oh, J. Yoo, J. Lee, *Macromol. Res.* **2023**, *31*, 1189.
[53] M. Zhu, P. Li, J. L. Li, T. Lei, *Mol. Syst. Des. Eng.* **2022**, *7*, 6.
[54] M. Ghittorelli, L. Lingstedt, P. Romele, N. I. Crăciun, Z. M. Kovács-Vajna, P. W. Blom, F. Torricelli, *Nat. Commun.* **2018**, *9*, 1441.
[55] C. Lee, C. Lee, S. Lee, J. Choi, H. Yoo, S. G. Im, *Nat. Commun.* **2023**, *14*, 3757.
[56] C. Pan, C. Y. Wang, S. J. Liang, Y. Wang, T. Cao, P. Wang, C. Wang, S. Wang, B. Cheng, A. Gao, E. Liu, *Nat. Electron.* **2020**, *3*, 383.
[57] B. J. Riley, C. L. Beck, J. S. Evarts, S. Chong, A. M. Lines, H. M. Felmy, J. McFarlane, H. B. Andrews, S. A. Bryan, K. C. McHugh, H. S. Cunningham, R. M. Asmussen, J. A. Dhas, Z. Zhu, J. V. Crum, S. D. Shen, J. S. McCloy, Z. M. Heiden, *AIP Adv.* **2024**, *14*, 080701.
[58] J. Lee, W. D. Lu, *Adv. Mater.* **2018**, *30*, 1702770.